Chemical Engineering Journal 306 (2016) 214–225

Contents lists available at ScienceDirect

Chemical Engineering Journal

journal homepage: www.elsevier.com/locate/cej

Production of spherical mesoporous molecularly imprinted polymer particles containing tunable amine decorated nanocavities with CO_2 molecule recognition properties

Seyed Ali Nabavi [b,a], Goran T. Vladisavljević [b,*], Eseosa M. Eguagie [b], Beichen Li [b], Stella Georgiadou [b], Vasilije Manović [a,*]

[a] Combustion and CCS Centre, Cranfield University, Cranfield MK43 0AL, United Kingdom
[b] Department of Chemical Engineering, Loughborough University, Loughborough LE11 3TU, United Kingdom

HIGHLIGHTS

- Spherical poly(AAm-co-EGDMA) particles with CO_2 recognition cavities were synthesized.
- Optimum ratio of acetonitrile to toluene in the organic phase was 30:70.
- Particles were thermally stable up to 240 °C as revealed by thermogravimetric analysis.
- CO_2 capture capacity reached 0.62 mmol/g at 25 °C and 0.15 bar CO_2 partial pressure.
- CO_2 capture capacity increased by increasing the density of CO_2-philic NH_2 groups.

GRAPHICAL ABSTRACT

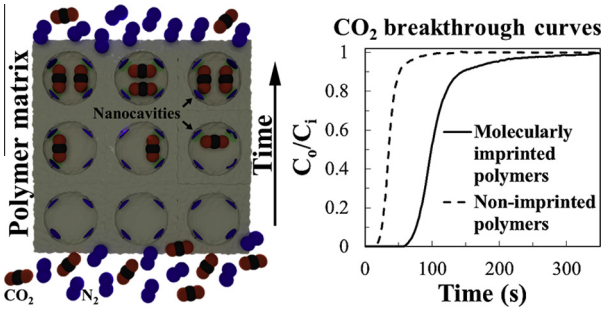

ARTICLE INFO

Article history:
Received 11 March 2016
Received in revised form 29 June 2016
Accepted 14 July 2016
Available online 16 July 2016

Keywords:
CO_2 recognition property
Molecularly imprinted polymer adsorbents
Amide decorated cavities
Post combustion carbon capture
Suspension polymerization
Dynamic CO_2 adsorption isotherms

ABSTRACT

Novel spherical molecularly imprinted polymer (MIP) particles containing amide-decorated nanocavities with CO_2 recognition properties in the poly[acrylamide-co-(ethyleneglycol dimethacrylate)] mesoporous matrix were synthesized by suspension polymerization using oxalic acid and acetonitrile/toluene as dummy template and porogen mixture, respectively. The particles had a maximum BET surface area, S_{BET}, of 457 m^2/g and a total mesopore volume of 0.92 cm^3/g created by phase separation between the copolymer and porogenic solvents. The total volume of the micropores (d < 2 nm) was 0.1 cm^3/g with two sharp peaks at 0.84 and 0.85 nm that have not been detected in non-imprinted polymer material. The degradation temperature at 5% weight loss was 240–255 °C and the maximum equilibrium CO_2 adsorption capacity was 0.56 and 0.62 mmol/g at 40 and 25 °C, respectively, and 0.15 bar CO_2 partial pressure. The CO_2 adsorption capacity was mainly affected by the density of CO_2-philic NH_2 groups in the polymer network and the number of nanocavities. Increasing the content of low-polar solvent (toluene) in the organic phase prior to polymerization led to higher CO_2 capture capacity due to stronger hydrogen bonds between the template and the monomer during complex formation. Under the same conditions, molecularly imprinted particles showed much higher CO_2 capture capacity compared to their non-imprinted counterparts. The volume median diameter (73–211 μm) and density (1.3 g/cm^3) of the produced particles were within the range suitable for CO_2 capture in fixed and fluidized bed systems.

* Corresponding authors.
E-mail addresses: g.vladisavljevic@lboro.ac.uk (G.T. Vladisavljević), v.manovic@cranfield.ac.uk (V. Manović).

http://dx.doi.org/10.1016/j.cej.2016.07.054
1385-8947/

1. Introduction

Excessive concentration of atmospheric CO_2, mainly because of extensive utilization of fossil fuels, has significantly contributed to global warming and requires immediate remedies [1,2]. Carbon capture and storage is the most viable short- to medium-term approach for decreasing the amount of CO_2 released into the atmosphere [3,4]. Carbon capture technologies can be classified into three main groups: oxy-fuel combustion, pre-combustion, and post-combustion carbon capture [5–9], the latter being the most practical approach to retrofit carbon capture onto existing power generation systems [4,9]. Post-combustion carbon capture by amine scrubbing is the most established technique for CO_2 capture from flue gases [10]. However, amines are corrosive and undergoes degradation on exposure to CO_2, O_2, SO_2, and heat, leading to increased costs and generation of products that are harmful to human health and the environment [1,11–15]. In addition, amine-based scrubbing systems require large volume, because of their low interfacial area per unit volume and high energy consumption for the solvent regeneration, decreasing the power output typically by 20–25% [16,17].

Solid CO_2 adsorbents are more efficient and environmentally friendly than amine solutions, because of their lower regeneration energy, high surface area per unit volume, and low volatility and corrosivity [16,18]. Zeolites are the most explored sorbents for post-combustion CO_2 capture with a very high CO_2 uptake and selectivity in some cases [19–21]. However, the presence of moisture in flue gases dramatically reduces their adsorption capacity and the desorption step must be carried out at higher temperatures [22,23].

Silica-based porous materials are associated with low CO_2 uptake, because of the low affinity of silica towards CO_2, but can readily be functionalized with amine groups [20,24–26], which exhibit a high affinity towards the molecules with a high quadrupole moment and polarizability. Amongst all the molecules present in post-combustion flue gases, CO_2 has the largest quadrupole moment and polarizability, which results in much higher CO_2 adsorption capacity of amine-functionalized adsorbents compared to their unmodified counterparts [27]. Amine groups can be incorporated into the silica surface through physical impregnation or covalent tethering [28–31]. Although impregnated silica materials exhibit lower cyclic stability than adsorbents with covalently tethered amines, both methods lead to a significant increase in CO_2 capture capacity, especially in the presence of moisture [15,32,33].

Metal organic frameworks (MOFs) have gained a lot of interest because of their high specific surface area, ease of structural tuning, narrow pore size distribution, and high CO_2 adsorption at elevated pressures [34]. However, they mostly suffer from low CO_2 adsorption at low pressures [35,36], low CO_2 selectivity, and significant deterioration in the presence of moisture, NO_x and SO_x [20,37]. Carbonaceous materials are another attractive type of adsorbents, because of their high surface area, tunable pore structure, low heat of adsorption, and low sensitivity to moisture and gas impurities [7,38]. Since CO_2 is adsorbed by physisorption, they suffer from a low CO_2 adsorption capacity under low pressure [2], which can be improved by potassium intercalation [39–41] and introduction of nitrogen functional groups [42,43]. The main disadvantage of highly porous materials, such as activated carbon and some MOFs is their low density, which can limit their application in fluidized bed reactors [7,39].

Polymer-based materials such as porous aromatic frameworks (PAFs), hyper cross-linked polymers (HCPs), and covalent organic polymers (COPs) [44–46] are a new class of CO_2 sorbents characterized by high selectivity and CO_2 uptake, hydrothermal stability and ease of structural modification. Polymeric adsorbents are usually produced as very fine particles that pack too tightly and can easily be entrained out of the bed. Therefore, they must be pelletized to be used in fluidized bed systems, which can block their reactive sites and reduce CO_2 adsorption capacity. Recently, molecularly imprinted polymer (MIP) particles for CO_2 capture with a separation factor of up to 340, insensitive to moisture, SO_2, NO, and O_2, have been synthesized by bulk polymerization [47,48]. Molecular imprinting creates template-shaped cavities within the polymer matrix with molecular recognition properties towards a specific target molecule [49]. However, bulk polymerization is not suitable for large-scale production. After polymerization, the bulk polymer is crushed, ground and sieved to obtain particles of the desired size range, which is time consuming, laborious, and only 30–40% of the ground polymer can be recovered. In addition, the particles produced by this method are susceptible to mechanical attrition because of their irregular shape and broad size distribution [49].

In suspension polymerization each monomer droplet acts as a tiny batch reactor, which facilitates heat transfer and thus, the polymerization occurs faster and the final conversion of the monomer can reach higher values [50]. Due to their spherical shape, the particles have a lower tendency to break down and their size can be finely tuned by controlling the operating conditions and phase compositions during emulsification [50]. In addition, the process is scalable and higher particle yields can be achieved due to the smaller amount of waste (off-specification) material.

In this work, novel spherical acrylamide-based MIP particles for CO_2 capture were fabricated by suspension polymerization in an oil-in-water (O/W) emulsion. Amide-decorated nanocavities were created by crosslinking acrylamide in the presence of oxalic acid, followed by extraction of the dummy template to expose nanocavities. The particles were inherently amide-functionalized and there was no need for amine grafting to increase CO_2 adsorption capacity. Due to CO_2-philic moieties on the walls of the cavities and their shape that is complementary to CO_2 molecules, the particles are highly selective to CO_2. They are suitable for use in fluidized bed reactors, because of their tunable diameter greater than 100 μm and relatively high density. The emulsion formulation and operating conditions were optimized to maximize CO_2 adsorption capacity of the particles in realistic post-combustion CO_2 capture situations.

2. Experimental section

2.1. Materials

Oxalic acid (OA), acrylamide (AAm), acetonitrile (AN), toluene (TL), methanol, and 0.1 M hydrochloric acid were supplied by Fisher Scientific, UK. Ethylene glycol dimethacrylate (EGDMA), azobisisobutyronitrile (AIBN), and polyvinyl alcohol (PVA, M_w = 13,000–23,000, 87–89% hydrolyzed) were purchased from Sigma Aldrich, UK. All the reagents were of analytical grade. Pure water was supplied using a Millipore Milli-Q Plus 185 water purification system. All the gases were supplied by BOC, UK with a purity higher than 99.999%.

2.2. Particle synthesis

O/W emulsions were prepared using the dispersed phase composed of OA (template), AAm (functional monomer), EGDMA (crosslinker), and AIBN (initiator) dissolved in a mixture of TL and AN (porogenic solvents). The continuous phase was a 0.1–1 wt% aqueous solution of PVA. Formulation parameters and polymerization conditions are shown in Table 1 and in the caption of Fig. 7. The particle synthesis involved four major steps, as follows:

Table 1
Summary of emulsion formulation and polymerization conditions of samples synthesized for CO_2 capture capacity measurements.[a]

Sample	AAm (g)	OA (g)	EGDMA (g)	AIBN (g)	Solvent (mL)		T_p (°C)	t_p (h)	ϕ_o (%)	Dv,0.5 (μm)	S_{BET} (m^2/g)	V_p (cm^3/g)	d_p (nm)
					AN	TL							
s.b.1	2.04	0.9	9.51	0.12	12	12	60	3	9	151	333	0.54	8.2
s.b.2	5.1	2.27	23.8	0.3	30	30	60	3	20	144	330	0.48	7.3
s.b.3	10.2	4.54	47.6	0.6	60	60	60	3	33	200	421	0.62	8.4
s.b.4	10.2	–	23.8	0.3	30	30	60	3	20	160	328	0.62	9.6
s.b.5	5.1	2.27	23.8	0.3	30	30	60	1	20	89	379	0.63	8.9
s.b.6	5.1	2.27	23.8	0.3	30	30	60	6	20	129	316	0.49	7.8
s.b.7	5.1	2.27	23.8	0.3	30	30	50	3	20	147	349	0.43	5.9
s.b.8	5.1	2.27	23.8	0.3	30	30	70	3	20	189	457	0.83	11.3
s.b.9	5.1	2.27	23.8	0.3	18	42	60	3	20	178	443	0.92	15
s.b.10	10.2	4.54	23.8	0.3	30	30	60	3	20	211	367	0.64	9.4
s.b.11	5.1	4.54	23.8	0.3	30	30	60	3	20	199	325	0.49	7.3
s.b.12	5.1	–	23.8	0.3	30	30	60	3	20	175	380	0.6	8.4
s.b.13	5.1	–	23.8	0.3	30	30	70	3	20	187	423	0.74	10.1
s.b.14	10.2	–	47.6	0.6	60	60	60	3	33	252	420	0.67	9.1
s.b.15	5.1	–	23.8	0.3	18	42	60	3	20	90	368	0.6	11.2

[a] T_p = polymerization temperature; t_p = polymerization time, ϕ_o = dispersed phase content; S_{BET} = specific surface area, V_p = total pore volume, d_p = average pore size. In all experiments the PVA concentration in the aqueous phase was 0.5 wt% and the stirring rate in the reactor was 200 rpm.

2.2.1. Step 1. Monomer-template self-assembly

The first step is self-assembly of functional monomer and template in a mixture of TL and AN and creation of monomer-template complex (Scheme 1, step I). Direct use of CO_2 as a template is impossible due to low solubility of CO_2 in organic solvents at ambient conditions. An alternative approach is to use a dummy template, here oxalic acid, which is a structural analog to the CO_2 molecule. Oxalic acid has a spatial structure very similar to two CO_2 molecules with their C atoms sitting back-to-back and O atoms pointing in opposite directions. The distance between adjacent NH_2 groups in the organic phase prior to polymerization was 0.45–0.7 nm [47] which is ideal for hydrogen bonding with CO_2 molecules, which have a kinematic diameter of 0.33 nm. OA and AAm were dissolved in the solvents and left overnight to ensure that molecular self-arrangement was fully completed.

2.2.2. Step 2. Suspension polymerization

The PVA solution was poured into a 500-mL jacketed reactor equipped with a four-neck lid and agitated using a four-bladed impeller with a diameter of 50 mm. (Fig. s.1). The organic phase was prepared by dissolving EGDMA and AIBN in a pre-mixed oxalic acid-AAm solution and emulsified in the reactor. After purging the reactor for 10 min with N_2 to remove oxygen, nitrogen blanketing was used to prevent oxygen from diffusing into the reactor. The temperature was raised using a water-recirculating heater/chiller system to initiate the polymerization (Scheme 1, step II). The same procedure was used for non-imprinted polymer particles (NIPs), except that no template was added in the organic phase.

2.2.3. Step 3. Surfactant removal

The surfactant was removed from the product suspension using two agitation methods, mechanical and ultrasonic agitation. In both methods the temperature of the wash water was kept at 85–90 °C for 5 min, followed by water extraction and addition of fresh hot water for the next wash cycle. The particle morphology and size distribution were determined after 4, 8, and 10 wash cycles by scanning electron microscopy (SEM) and dynamic light scattering using a Malvern Mastersizer S (Malvern Instruments, UK) particle size analyzer.

2.2.4. Step 4. Template removal

The template was removed by washing the particles several times with a 1:9 (v/v) mixture of hydrochloric acid and methanol, until no oxalic acid was detected in the rinses by a Lambda 35 UV/VIS spectrometer (PerkinElmer, US). The extraction of the template from the particles resulted in formation of nanocavities decorated with covalently attached amide groups (Scheme 1, step III). In addition, mesopores were formed in the polymer matrix due to phase separation between the polymer and the solvents during the polymerization process.

2.3. Material characterization

2.3.1. Scanning electron microscopy (SEM)

The particle morphology was analyzed using a TM3030 benchtop scanning electron microscope (Hitachi, Tabletop Microscope Europe) operating at an accelerating voltage of 15 keV. The sam-

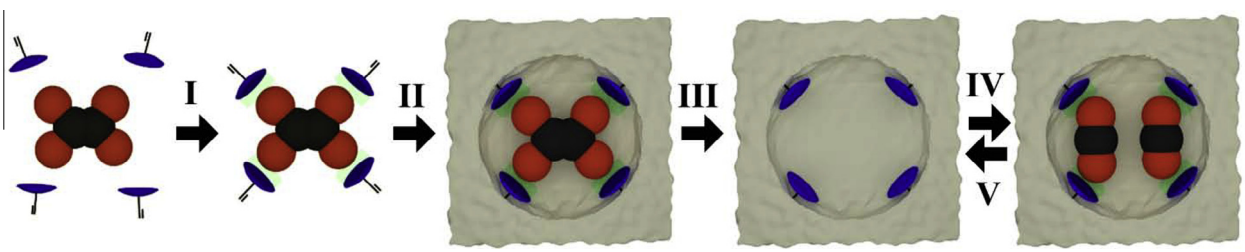

Scheme 1. A synthesis of molecularly imprinted polymer particles in this work. I: OA-AAm self-assembly via hydrogen bonding and formation of pre-polymerization complex in the organic phase; II: polymerization with EGDMA; III: template removal, IV/V: adsorption/desorption of CO_2 molecules within the nanocavity. Oxygen, carbon, and nitrogen atoms are shown in red, black, and blue, respectively, and green areas represent the hydrogen bonding interactions. (For interpretation of the references to colour in this scheme legend, the reader is referred to the web version of this article.)

ples were coated with gold/palladium (80/20) prior to the SEM to prevent accumulation of electrostatic charges on the particles. The sputtering rate was 0.85 nm per second at 2 kV and 25 mA of plasma current.

2.3.2. Particle size distribution

The particle size distribution was measured using a laser diffraction particle size analyzer, Malvern Mastersizer S (Malvern Instruments, UK). The mean particle size was expressed as the volume median diameter, Dv,0.5, which is the diameter corresponding to 50% on the cumulative volume distribution curve. The degree of particle size uniformity was expressed as relative span:

$$\text{span} = \frac{Dv,0.9 - Dv,0.1}{Dv,0.5} \quad (1)$$

where Dv,0.1 and Dv,0.9 are the diameters on the cumulative volume distribution curve corresponding to 10% and 90%, respectively.

2.3.3. Pore size analysis

The pore size analysis was performed using a Micromeritics ASAP 2020 HD Accelerated Surface Area and Porosimetry System at 77 K in a liquid nitrogen bath. The samples were degassed at 80 °C overnight prior to the analysis. The specific surface area was calculated by the Brunauer–Emmett–Teller (BET) method over the relative pressure range, P/P_0, of 0.06–0.3. The mesopore size distribution was determined using the Barrett-Joyner-Halenda (BJH) model and the total pore volume was calculated from the amount of N_2 adsorbed at P/P_0 of 0.99. The size distribution of micropores and the total pore volume of micropores were measured using the Horvath–Kawazoe (HK) model at P/P_0 smaller than 10^{-2}.

2.3.4. Density measurement

The particle density was measured using a helium pycnometer 9200 (Micromeritics, US). The particles were dried overnight at 80 °C prior to the measurement. For each test, five runs were performed and the average value was reported.

2.3.5. Thermal analysis

The thermal stability of the CO_2-MIP particles was characterized using a thermogravimetric analyzer (TGA) Q5000IR (TA Instruments, US) under a nitrogen flow rate of 20 mL/min by heating 10–20 mg of sorbents from 50 to 600 °C at a ramp rate of 10 °C/min.

2.3.6. X-ray photoelectron spectroscopy (XPS)

XPS was performed on a K-ALPHA spectrometer (Thermo Scientific, UK) using monochromatic Al Kα X-rays (36 W, 400 μm spot size) and low-energy electron/ion flooding for charge compensation. Survey scan spectra for elemental analysis were obtained using a pass energy of 200 eV, a step size of 1 eV, a dwell time of 10 ms and 15 scans. High-resolution scans of the C 1s, O 1s and N 1s peaks were acquired using a pass energy of 50 eV and a step size of 0.1 eV with a dwell time of 50 ms and 10 scans.

2.3.7. Fourier transform infrared (FTIR) spectroscopy

The FTIR spectra were measured over the range of 500–4000 cm^{-1} using a Thermo Scientific Nicolet iS50 ATR spectrometer with a monolithic diamond crystal. The samples were placed on the Universal diamond ATR top-plate and the spectrum was recorded within 32 s.

2.3.8. Dynamic CO_2 adsorption experiments

CO_2 adsorption on the synthesized particles was investigated in a fixed-bed column made of stainless steel (Fig. 1). In each test the column (15.8 mm O.D. and 9.25 mm I.D.) was loaded with 2.5-3 g of the particles sieved using a 0.075 mm stainless steel mesh. After loading, 0.035-mm stainless steel mesh and quartz wool plug were placed on either side of the bed to retain the particles. An in-house temperature controller was used to provide a uniform temperature along the column. The gas flow rate through the system was controlled using a mass flow controller (Alicat Scientific Inc, UK). Prior to each adsorption test, the particles were purged with N_2 for 2 h at 120 °C and 130 mL/min. The column was then sealed on both sides and left to cool down to the pre-determined adsorption temperature followed by blowing the feed stream composed of 15 vol% CO_2 and 85 vol% of N_2 through the bed at 130 mL/min. A CO_2 infrared analyzer (Quantek Instruments, USA) was used to continuously monitor the CO_2 concentration in the outlet stream. The CO_2 breakthrough curves were corrected by subtracting the mean resistance time of the gas stream (58 s at 130 mL/h and 40 °C), which was measured by flowing the feed gas mixture through the empty column.

3. Results and discussion

3.1. Production and characterization of particles

In O/W suspension polymerization, the organic phase, containing the template, the monomer, the cross-linker, and the initiator dissolved in the solvent(s), is dispersed in the aqueous surfactant solution. The droplets are converted to spherical polymer beads through a free radical polymerization. During the emulsification step, the surfactant forms a protective film at the interface preventing droplet coalescence. After polymerization, the surfactant must be removed to minimize particle agglomeration, since it results in a significant reduction in the surface area and CO_2 adsorption capacity. Fig. 2 shows the effect of two different particle agitation methods (ultrasound and mechanical) during washing on the morphology and size distribution of the particles after 4, 8, and 10 wash cycles. On the SEM images, it can be seen that after 8 and 10 wash cycles the particles agitated using ultrasound were considerably less agglomerated than mechanically agitated particles, and it was confirmed by the lower Dv,0.5 and span values. After 10 ultrasound treatments, almost no agglomerated particles were detected. Therefore, particle washing using 10 repeated ultrasound treatments was implemented as a standard procedure in the subsequent work.

The physisorption data obtained from liquid nitrogen adsorption/desorption curves are presented in Figs. 3–5 and the corresponding specific surface areas, S_{BET}, specific pore volumes, V_p, and average pore sizes, d_p, are listed in Table 1. The majority of the samples follow a type IV nitrogen adsorption/desorption isotherm, featured by a hysteresis loop attributed to capillary condensation in mesopores (Fig. 3). Therefore, the material can be classified as a mesoporous adsorbent. However, for s.b.9 despite the presence of a slight hysteresis loop, the pore size distribution was wide and went beyond 50 nm implying a Type II isotherm profile. Compared to bulk polymerization [47], suspension polymerization led to more uniform mesopore size distribution. In addition, all samples synthesized by bulk polymerization followed a Type II isotherm with an average pore size of 10–24 nm, as compared with 5–15 nm found in this work (Table 1). The S_{BET} values in this work were 316–457 m^2/g, compared with 80–258 m^2/g reported in bulk polymerization. Moreover, the maximum pore volume of 0.92 cm^3/g for the sample b.9 (Table 1) was considerably higher than the maximum V_p value in bulk polymerization.

Since imprinted nanocavities are smaller than 2 nm, the Horvath–Kawazoe (HK) method was used to compare the size distribution of the micropores ($d < 2$ nm) in the MIP sample s.b.10 and the NIP material s.b.4, Fig. 5. Both samples were prepared under the same conditions, except that no template was used in s.b.4.

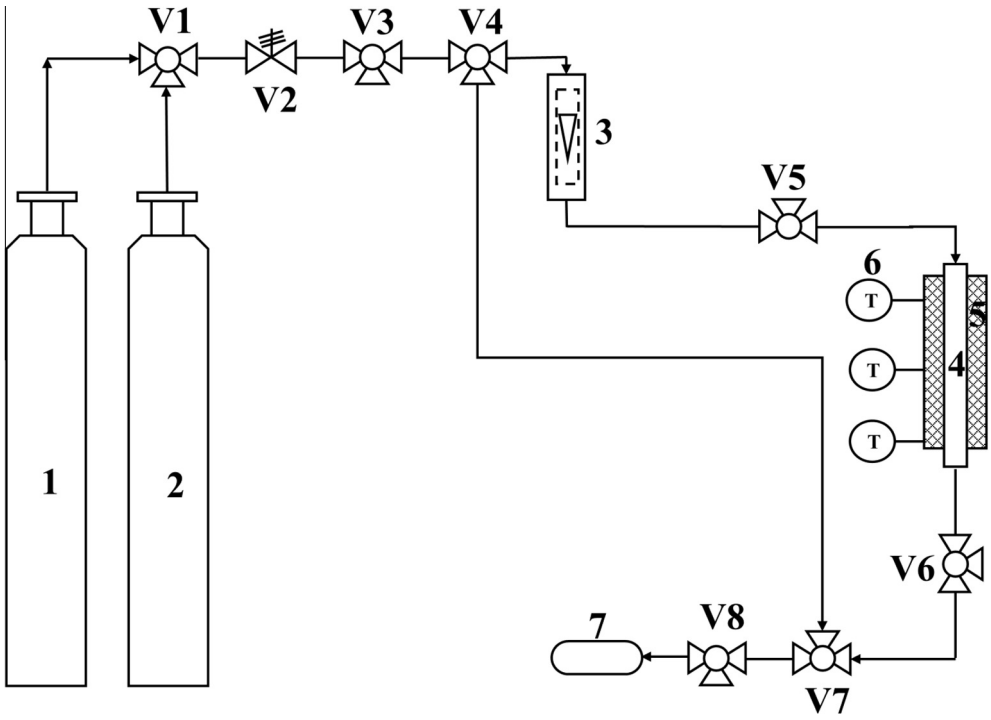

Fig. 1. A schematic of the fixed-bed system for CO_2 adsorption: (1) CO_2 cylinder; (2) N_2 cylinder; (3) mass flow controller; (4) fixed-bed column; (5) heating system; (6) thermocouples; (7) CO_2 gas analyzer; (V1 & V3–V8) 3-way valves; (V2) pressure relief valve.

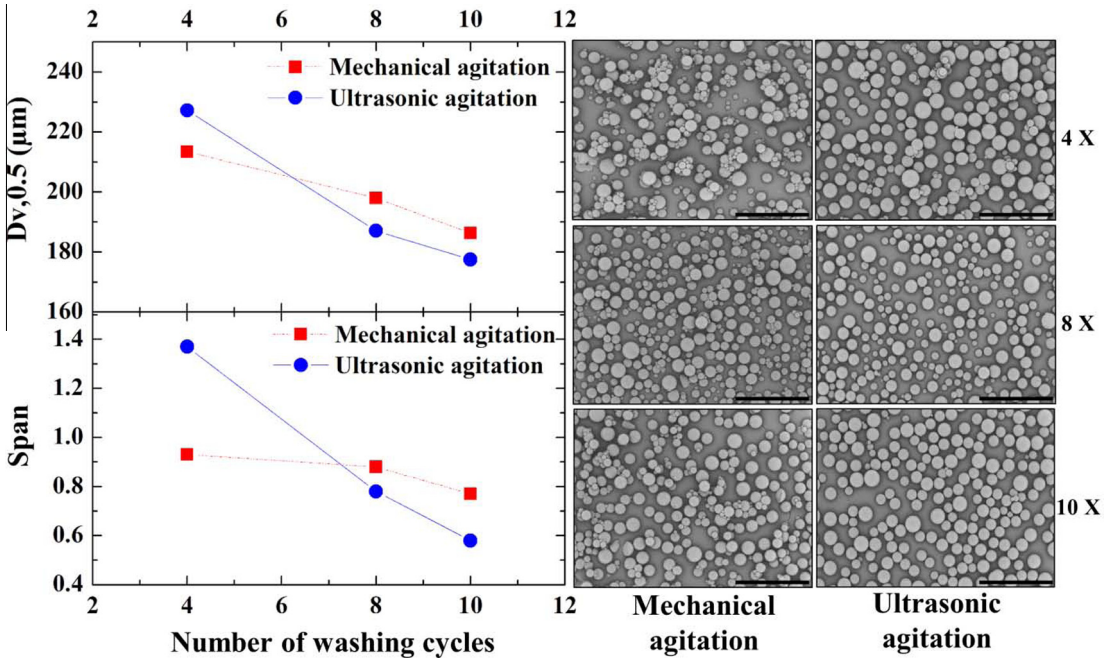

Fig. 2. Comparison of two particle washing procedures based on mechanical and ultrasound agitation: (Left) The variation of volume median particle diameter and particle uniformity with the number of wash cycles; (Right) SEM images of the particles after 4, 8, and 10 wash cycles. All scale bars are 1 mm.

There were two sharp distinct peaks for s.b.10 at 0.84 and 0.85 nm and both were significantly larger than the ones for s.b.4, implying the presence of nanocavities in the MIP matrix. In addition, the total pore volume in the micro-range (pore diameter <2 nm) was 0.1 cm^3/g for s.b.10 and only 0.06 cm^3/g for s.b.4. The better structural properties of s.b.10 as compared with s.b.4 were confirmed by CO_2 capture measurements. The CO_2 capture capacity of MIP particles was 2.5 times higher than that of NIP particles (Fig. 8c), which can be attributed to the nanocavities in the imprinted polymer matrix.

To further verify the better performance of MIPs, five additional MIP/NIP pairs were analyzed. The performance of MIPs was assessed using the standard protocol based on the imprinting factor, IF, which is the ratio of equilibrium adsorption capacity of MIP to its corresponding NIP particles [51,52]. For the five MIP/NIP pairs (s.b.2 vs. s.b.12, s.b.3 vs. s.b.14, s.b.8 vs. s.b.13, s.b.9 vs. s.

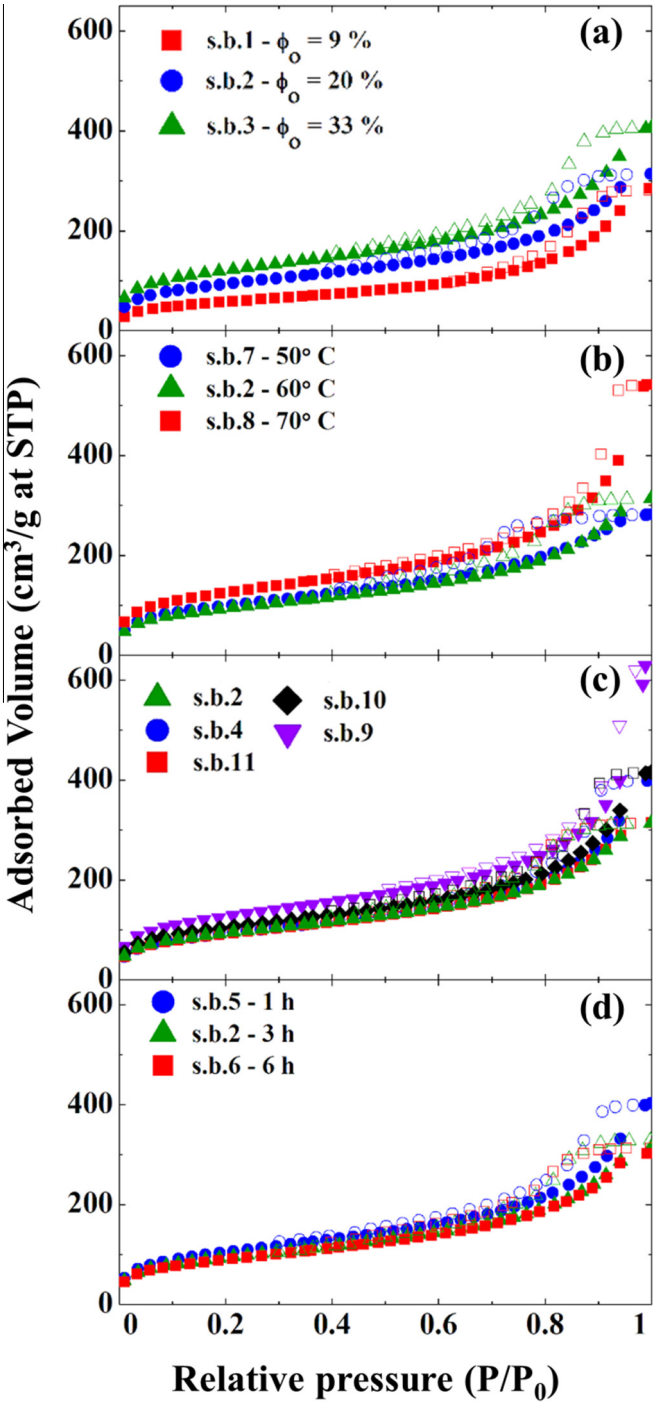

Fig. 3. Nitrogen adsorption-desorption isotherms of the samples as a function of: (a) the dispersed phase content; (b) polymerization temperature; (c) molecular imprinting, solvent content, and monomer concentration; (d) polymerization time. The solid symbols represent the adsorption isotherms and the open symbols represent the desorption curves.

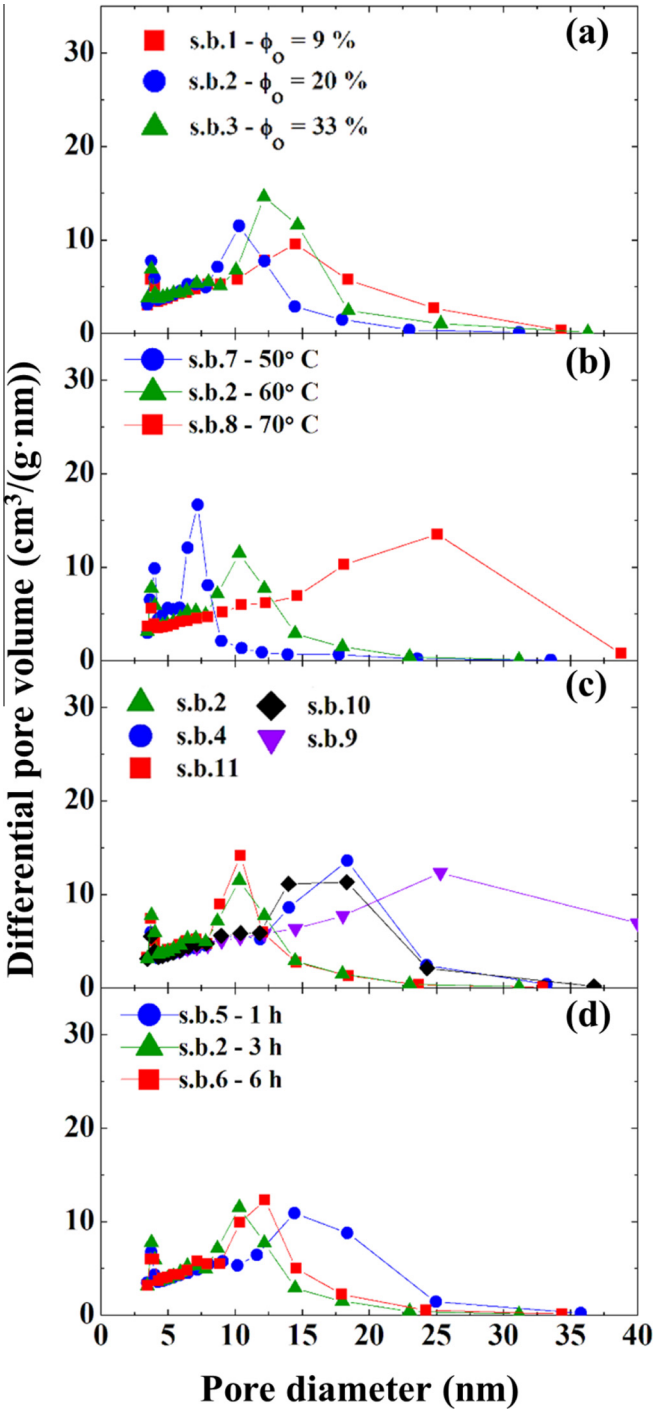

Fig. 4. Mesopore size distribution curves for the samples. The variable parameter: (a) dispersed phase content; (b) polymerization temperature; (c) template concentration, solvent content, and monomer concentration in the organic phase; (d) polymerization time.

b.15, and s.b.11 vs. s.b.12), the CO_2 capture capacity was measured (Fig. 8), and the corresponding IFs were found to be 2.3, 1.9, 1.5, 3.7, and 1.3 respectively. In all cases, IF was greater than 1, implying higher binding affinity of MIPs compared to NIPs. Since MIPs synthetized using bulk polymerization had an IF of 1.1 [47], it is clear that the current MIPs produced by suspension polymerization shows a higher binding affinity towards CO_2 molecules.

Although the pore volume in the micropore range for the MIPs is larger than that for the NIPs, the total pore volume and S_{BET} surface area can be mainly attributed to the presence of mesopores formed due to phase separation between the polymer and the solvents during the polymerization process, particularly for polymeric particles with large pore volumes. Although the role of template in the creation of nanocavities is known, the effect of template on the structure of mesopores is not well understood and is beyond the scope of this study. Comparing the total pore volume and S_{BET} surface area of MIP samples and their NIP counterparts in Table 1, no specific trend was observed, and both smaller and larger pore volumes of NIPs were found in some cases. The same observation was reported by Dirion et al. [51], who developed a library of

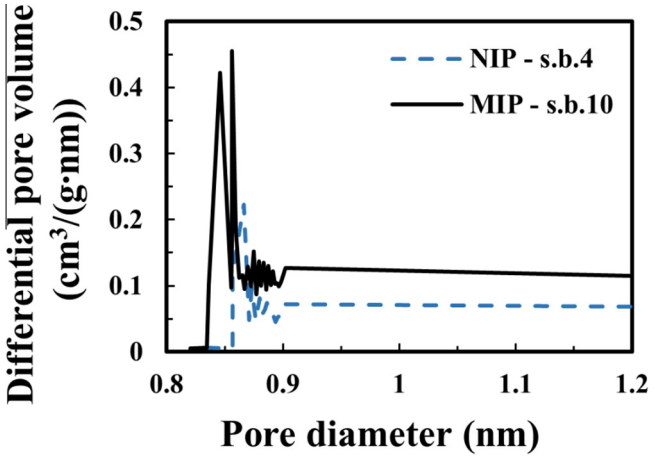

Fig. 5. Comparison of micropore size distributions for molecularly imprinted and non-imprinted polymer particles, s.b.10, and s.b.4 respectively, using Horvath–Kawazoe (HK) model.

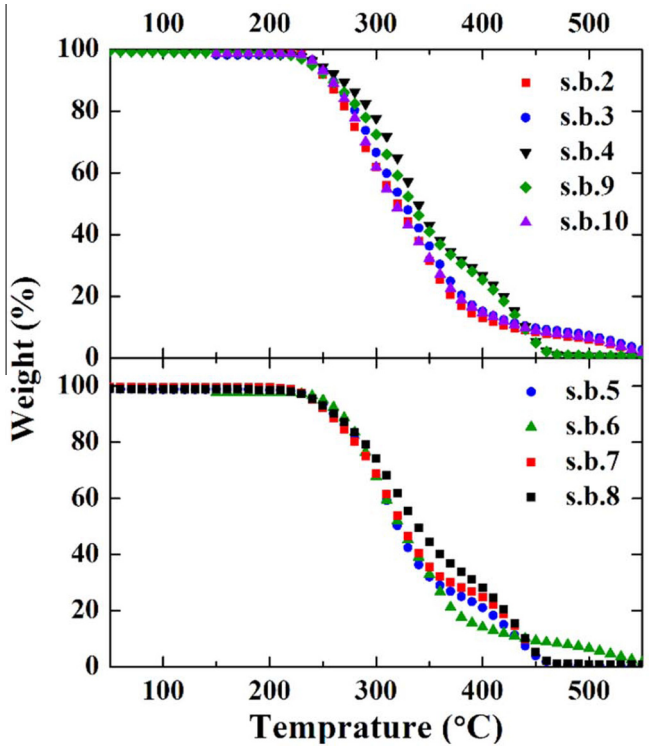

Fig. 6. The TGA curves of the samples over the temperature range of 50–600 °C at a temperature ramp rate of 10 °C/min and under nitrogen flow.

MIP sorbents for use in pure aqueous environments. Therefore, it might not be possible to evaluate the separation performance of MIP and NIP particles by comparing their total pore volume and S_{BET} surface area.

Fig. 6 shows the TGA curves for selected samples. All TGA curves have similar patterns with no weight loss up to 220 °C and the thermal decomposition temperature corresponding to 5% weight loss occurring at 240–255 °C. The average density of the particles measured using a multivolume helium pycnometer was 1.3 g/cm^3.

3.2. Particle size control

Inappropriate particle size can considerably limit the applicability of solid sorbents. Particles with very small sizes can cause large pressure drops in fixed bed reaction systems [53]. In fluidized bed reactors, small particles belonging to Group C according to the Geldart classification [54] are prone to cohesion, which may result in channeling at high flue gas flow rates, and reduced capture efficiency [55]. On the other hand, large particles (Group D) have a low surface area-to-volume ratio, resulting in a lower diffusion rate of CO_2 within the particle. Therefore, particles for CO_2 capture in fluidized beds should be large Group A particles or small Group B particles [55,56]. Based on the particle density in this work (1.3 g/cm^3), their smallest size must be about 120 μm to fall under these categories. The particle size was controlled by changing the agitation rate in the reactor and the concentration of surfactant in the aqueous phase. The effect of agitation speed on the mean droplet size at two different dispersed phase contents, ϕ_o, is shown in Fig. 7a and b. At ϕ_o = 9%, an increase in stirring rate from 100 to 600 rpm caused a decrease in the droplet size from 171 to 73 μm. At ϕ_o = 20%, an opposite trend was observed and an increase in agitation speed led to an increase in the droplet size. In stirred vessels, there are two factors that determine the particle size of an emul-

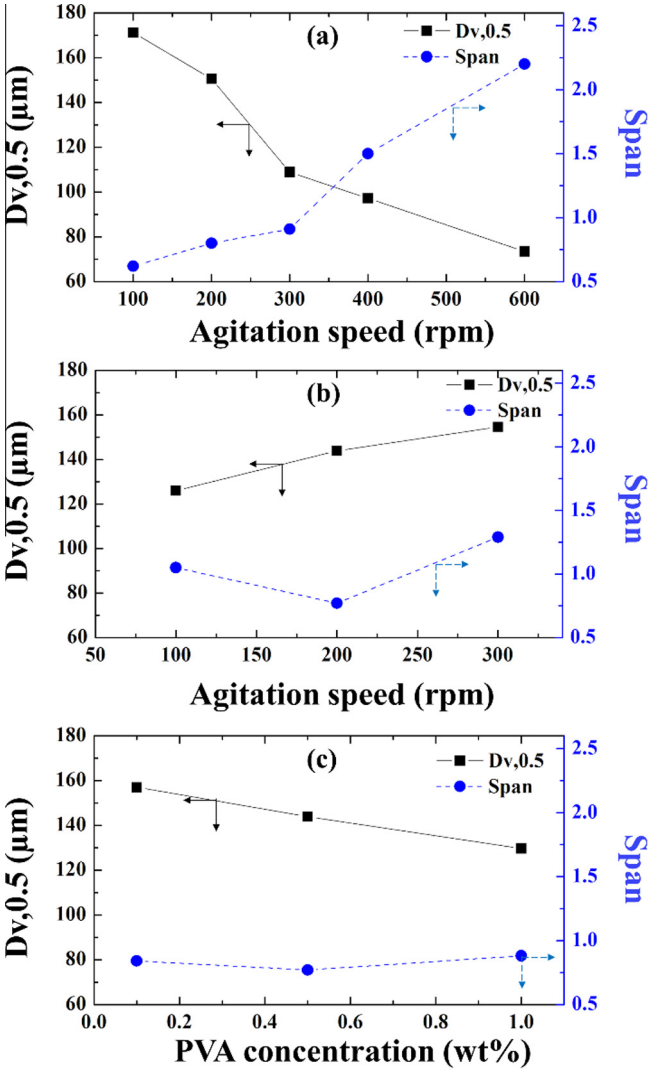

Fig. 7. The effect of dispersed phase content, ϕ_o, stirring rate, ω, and PVA concentration in the aqueous phase, C_{PVA}, on the median droplet diameter and the span: (a) ϕ_o = 9 vol%, C_{PVA} = 0.5 wt%, 2.04 g AM, 0.9 g OA, 9.51 g EGDMA, 0.12 g AIBN, 12 mL TL, 12 mL AN; (b) ϕ_o = 20 vol%, C_{PVA} = 0.5 wt%, 5.1 g AM, 2.27 g OA, 23.8 g EGDMA, 0.3 g AIBN, 30 mL TL, 30 mL AN; (c) ϕ_o = 20 vol%, ω = 200 rpm, 5.1 g AM, 2.27 g OA, 23.8 g EGDMA, 0.3 g AIBN, 30 mL TL, 30 mL AN. In all experiments T_p = 60 °C and t_p = 3 h.

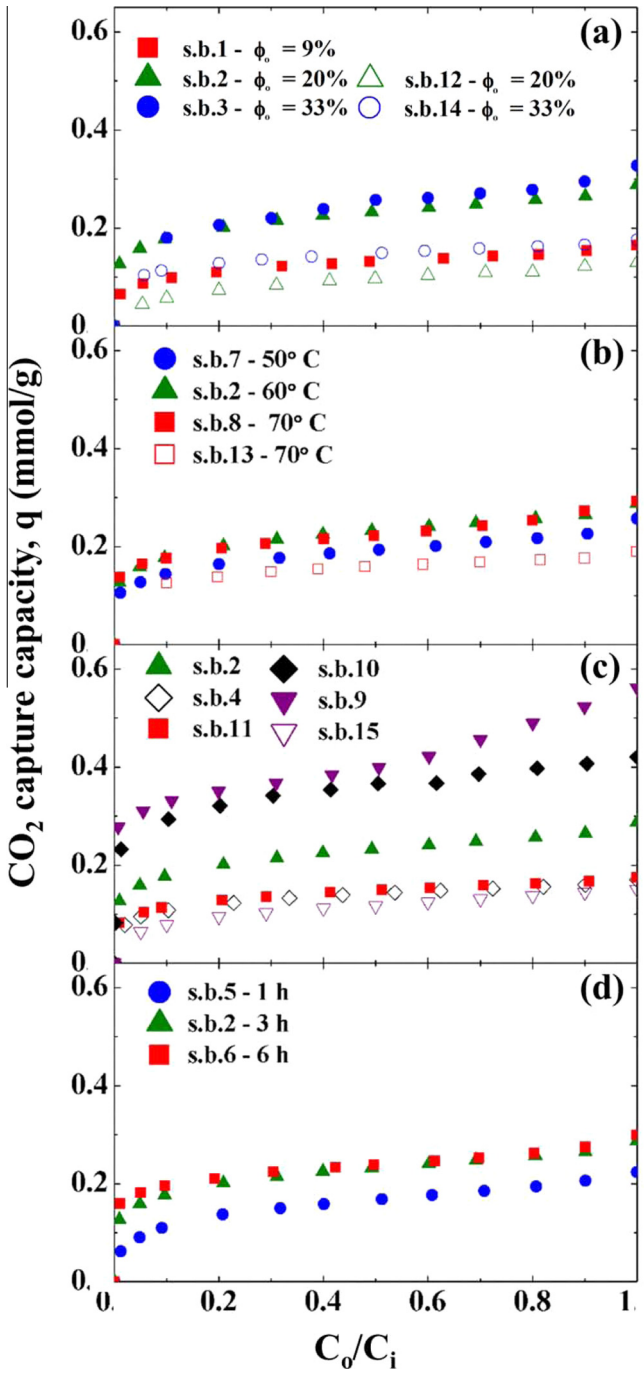

Fig. 8. The CO_2 adsorption capacity of the samples listed in Table 1 calculated from the breakthrough curves using Eq. (2). The variable parameter: (a) disperse phase volume fraction; (b) polymerization temperature; (c) template concentration, solvent content, and monomer concentration in the organic phase; (d) polymerization time. The adsorption temperature was 40 °C and the gas flow rate was 130 mL/min for all runs. For (a–c) the filled symbols represent MIP samples, and the empty symbols represent the corresponding NIP samples.

sion: droplet breakage due to viscous and/or inertial forces, and droplet coalescence, due to droplet collision. At low ϕ_o values, the droplet breakup is a dominant factor controlling the droplet size, and an increase in the agitation speed results in higher shear forces exerted by the impeller on the droplets and their fragmentation into smaller droplets. At higher ϕ_o values, droplet coalescence dominates over droplet breakup and consequently leads to larger droplets at higher stirring rates. The latter behavior is common in industrial suspension polymerization processes, where the dispersed phase content is relatively high [50]. At ϕ_o = 9 vol%, the particles fabricated at 100–300 rpm were rather uniform in size with a span of 0.6–0.91 (Fig. 7a). On the other hand, at 400–600 rpm the particles were highly polydispersed with a span of up to 2.2. At ϕ_o = 20%, the particle size distribution was independent of the stirring rate and the span varied between 0.77 and 1.29.

The effect of the concentration of PVA in the continuous aqueous phase on the particle size is shown in Fig. 7c. As expected, the median particle size decreased on increasing the PVA concentration from 0.1 to 1 wt%. At the higher PVA concentration, the amount of surfactant adsorbed on the surface of the droplets is higher, which reduces the interfacial tension and lowers the required energy for droplet disruption. Therefore, for a constant energy input, smaller droplets were formed at higher PVA concentration. The most uniform droplets (span = 0.77) were produced at 0.5 wt% PVA, which is a typical surfactant concentration in suspension polymerization. Also, at 1 wt% PVA in the aqueous phase it is more difficult to remove PVA after polymerization. Therefore, 0.5 wt% was considered as the optimum PVA concentration.

3.3. CO_2 adsorption capacity of synthesized particles

The CO_2 adsorption capacity, q, of the samples from Table 1 was measured in the fixed bed column shown in Fig. 1 and calculated using the following equation [57]:

$$q = \frac{QC_i t_{ad}}{m_s} \quad (2)$$

where q (mmol/g) is the CO_2 adsorption capacity, Q (mL/min) is the feed gas flow rate upstream of the column, m_s (g) is the mass of the particles in the column, and C_i (mmol/mL) is the concentration of CO_2 in the feed stream calculated using Eq. (3):

$$C_i = \frac{n_i P}{RT} \quad (3)$$

where n_i is the molar fraction of CO_2 in the feed gas ($n_i = 0.15$), P (kPa) is the total pressure of the gas stream (~102 kPa), T (K) is the adsorption temperature, R is the universal gas constant, 8.314 J/(K·mol), and t_{ad} is the stoichiometric time, which is equal to the breakthrough time in an ideal adsorption column with a vertical breakthrough curve, i.e., in a column operating at 100% CO_2 removal efficiency until the particles are fully saturated with CO_2. The t_{ad} value corresponds to the area between the breakthrough curve and the vertical axis (C_o/C_i) and can be calculated as:

$$t_{ad} = \int_0^t \left(1 - \frac{C_o}{C_i}\right) dt \quad (4)$$

where C_o (mmol/mL) is the CO_2 concentration in the effluent stream and t (min) is the time. The CO_2 adsorption capacity for different samples over the range of C_o/C_i from 0 to 1 is shown in Fig. 8. The particles were evaluated based on their equilibrium CO_2 adsorption capacity, q_{eq}, which is a q value corresponding to $C_o/C_i = 1$. It occurs when the effluent concentration reaches the feed gas concentration, and the material is no longer capable of adsorbing CO_2.

The effect of polymerization temperature over the range of 50–70 °C is shown in Fig. 8b. To achieve a sufficient decomposition rate of AIBN, the polymerization temperature should be at least 50 °C. At the start of the polymerization process, individual polymer particles (nuclei) grow separately inside organic phase droplets. These nuclei eventually agglomerate via inter-nuclei crosslinking and the final porous bead is formed. The higher the polymerization temperature, the higher the polymerization rate [58] and the larger the number of nuclei formed. The size of individual polymer particles in the bead decreases on increasing number of nuclei, which

should result in higher surface area of the bead. Indeed, the highest surface area in Table 1 (457 m^2/g) corresponds to the beads synthesized at 70 °C. However, higher temperatures can weaken monomer-template interactions and reduce the quality of active sites in the polymer network. As a result, q_{eq} had similar values for the particles synthesized at 60–70 °C (0.26–0.29 mmol/g).

The effect of molecular imprinting on CO_2 adsorption capacity is shown in Fig. 8c for samples s.b.10 and s.b.4 prepared under the same conditions except that oxalic acid was added in the organic phase in sample s.b.10. As a result, q_{eq} for s.b.10 was 0.42 mmol/g, as compared to 0.17 mmol/g for the NIP sample s.b.4, which confirms that molecular imprinting improves CO_2 adsorption capacity. The high affinity of MIP particles towards CO_2 can be attributed to a combination of size exclusion effect on gas molecules, which is based upon their size and shape, and dipole-dipole interactions between CO_2 molecules and CO_2-philic NH_2 moieties inside the cavities. The cavity architecture (size and shape) facilitates the entrapment of CO_2 molecules in the polymer matrix due to structural compatibility of the cavities and CO_2 molecules. In addition, larger quadrupole moment and polarizability of CO_2 molecules compared to N_2 molecules (2.85 to 1 and 1.5 to 1, respectively) enhance the affinity of protic NH_2 groups on the cavity walls towards the CO_2 molecules leading to higher CO_2 uptake.

The effect of template concentration and solvent ratio in the organic phase on CO_2 adsorption capacity can be seen in Fig. 8c. When the monomer-to-template ratio was reduced from 2.25:1 to 1.12:1, a decrease in q_{eq} from 0.29 to 0.17 mmol/g was observed (samples s.b.11 and s.b.2), probably due to a smaller number of NH_2 groups per cavity. When the volume ratio of AN to TL was reduced from 50:50 to 30:70, an increase in q_{eq}, S_{BET}, and V_p was observed (samples s.b.2 and s.b.9). It is known that apolar, nonprotic solvents, such as toluene, stabilize hydrogen bonds and maximize the likelihood of complex formation between the template and the monomer, which leads to a larger number of cavities and enhanced affinity of MIPs towards the target molecules [59]. A polarity index of TL (2.4) is lower than that of AN (5.8), which allows stronger template-monomer interactions in a pre-polymerization solution. On the other hand, toluene is considered as a bad solvent for AAm and a certain amount of good solvent (AN) must be added to ensure that the organic phase is homogeneous. Increasing the level of bad solvent can cause early phase separation between the polymer and the solvents which results in aggregation of copolymer nuclei into larger clusters [59,60], hence, the pore size and pore volume increase (Fig. 4c and Table 1). Increased particle porosity can facilitate the diffusion of CO_2 through the polymer matrix, resulting in a higher CO_2 adsorption capacity for sample s.b.9 compared with s.b.2 (Fig. 8c).

Fig. 8d shows the effect of polymerization time on the CO_2 adsorption of synthesized particles over the range of 1–6 h. The difference in q_{eq} for the samples produced after 3 and 6 h was negligible (0.29 and 0.30 mmol/g, respectively). However, q_{eq} for the particles prepared after 1 h was 0.22 mmol/g, due to low conversion of AAm and a loss of active sites. Since the difference in q_{eq} for the particles synthesized after 3 and 6 h was negligible, 3 h was considered sufficient time for polymerization and used for the majority of samples in Table 1.

The effect of dispersed phase content, ϕ_o on CO_2 adsorption capacity is shown in Fig. 8a. An increase in ϕ_o from 9 to 33% resulted in an increase in q_{eq} from 0.17 to 0.32 mmol/g. It can be explained by the lower amount of acrylamide diffused from the organic phase droplets to the aqueous phase during polymerization, leading to the higher amount of NH_2 groups in the polymer network and the higher number of cavities in the polymer matrix. The diffusion of AAm was suppressed at higher ϕ_o values, because of the smaller amount of aqueous phase in the reactor. The mass fraction of nitrogen on the surface of the particles was quantified using XPS, as shown in Fig. 9a. In the samples prepared under the same operating conditions and using the same organic phase (s.b.1, s.b.2, and s.b.3), the nitrogen content increased on increasing ϕ_o, due to an increasing amount of NH_2 groups on the particle surface. Therefore, the main parameter affecting the CO_2 adsorption capacity is the density of NH_2 active sites on the surface, rather than specific surface area or total pore volume. This conclusion can be confirmed by comparing the nitrogen content and q_{eq} for two samples, s.b.10 and s.b.2, prepared under the same conditions, but the concentration of template and monomer was doubled in s.b.2. As shown in Fig. 9, the nitrogen fraction of s.b.10 was 2.4 times larger than that in s.b.2 and as a result, q_{eq} was 1.5 times larger than that of s.b.10 (Fig. 8c). The same trend was reported in bulk polymerization with higher surface density of NH_2 groups leading to higher CO_2 adsorption [47].

The FTIR spectra of s.b.1, s.b.2, s.b.3, and s.b.10 samples are shown in Fig. 9b. The peak at around 3440 cm^{-1} on all spectra

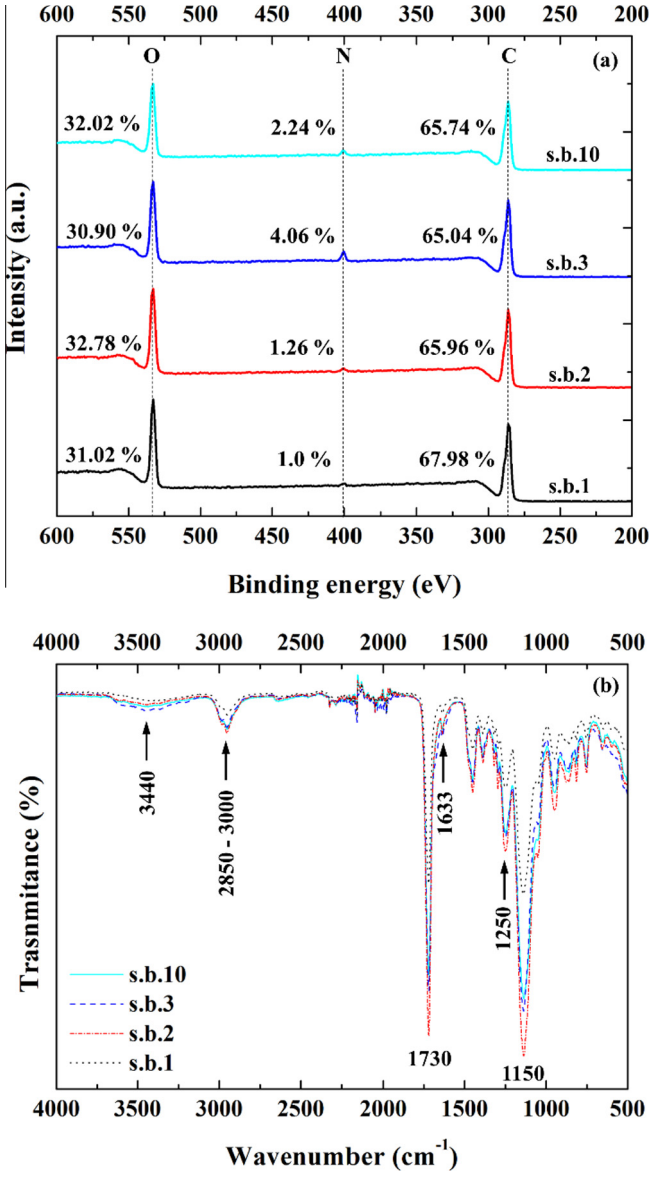

Fig. 9. Surface chemical analysis and FTIR analysis of samples b.1, b.2, b.3 and b.10: (a) XPS spectra and the mass percent of carbon, oxygen, and nitrogen; (b) FTIR spectra.

can be attributed to amine N–H stretching vibrations. The most intense N–H stretching peak was obtained for s.b.3, followed by s.b.10, s.b.2, and s.b.1, which corresponds to the fraction of nitrogen on the surface found by XPS. Almost the same sequence of peaks was observed at 1663 cm^{-1} which can be attributed to N–H bending vibrations. The two peaks at 1150 cm^{-1} and 1250 cm^{-1} are due to C–N stretching vibration. Therefore, the results imply the presence of amine groups on the surface of synthesized adsorbents. The peak at 1730 cm^{-1} can be attributed to C=O bonds in AAm and EGDMA, and the peaks at 2850–3000 cm^{-1} are due to C–H stretching vibration. There is no peak in the range of 1680–1640 cm^{-1} corresponding to C=C stretch in EGDMA and AAm, meaning there is no monomer or crosslinker left in the polymer particles and all carbon-carbon double bonds are broken. The peaks over the range of 910–665 cm^{-1} could be attributed to N–H wagging vibration.

Although the CO_2 adsorption capacity is higher at higher AAm concentration in the organic phase, AAm partitions between aqueous and organic phase. Excessive concentration of AAm in the aqueous phase results in gel formation in the continuous phase and failure of particle synthesis. For each ϕ_o value it is vital to find the highest possible concentration of AAm in the organic phase that will not cause gelation of the aqueous phase. A phase diagram of ϕ_o vs. C_{AAm} is shown in Fig. 10, and the safe region, where no gelation occurred, is highlighted in green.

The effect of temperature on q for s.b.9 is shown in Fig. 11. As expected, a considerable decrease in q_{eq} from 0.62 mmol/g to 0.28 mmol/g was observed, as the temperature increased from 25 °C to 80 °C, which can be attributed to the exothermic nature of the adsorption process and weakened hydrogen bond interactions between CO_2 and NH_2 groups at higher temperatures. In comparison with the existing polymeric adsorbents at low CO_2 partial pressures, the current MIPs showed very good CO_2 capture capacity, which was larger than the maximum CO_2 capture capacity of conjugated microporous polymer (CMP) networks developed by Dawson et al. [61] (0.3 mmol/g at 0.15 bar and 25 °C), microporous organic polymers (MOPs) produced by Kaliva et al. [62] (0.2 mmol/g at 0.15 bar and −5 °C), and azo-covalent organic polymers (azo-COPs) synthesized by Patel et al. [63] (0.4 mmol/g at 0.15 bar and 25 °C). The CO_2 capture capacity of the current MIPs was comparable to that of nanoporous organic polymers (NOPs)

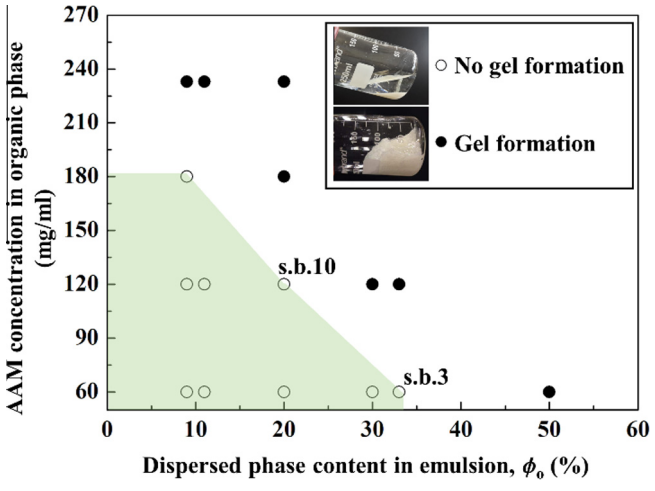

Fig. 10. The phase diagram of acrylamide gelation based on AAm concentration in the organic phase and volume percent of the dispersed phase in emulsion. T_p = 60 °C, t_p = 3 h, ω = 200 rpm for all the experiments. The green area represents the conditions where no gel formation occurred. Solid black circles are the conditions that resulted in gel formation. (For interpretation of the references to colour in this figure legend, the reader is referred to the web version of this article.)

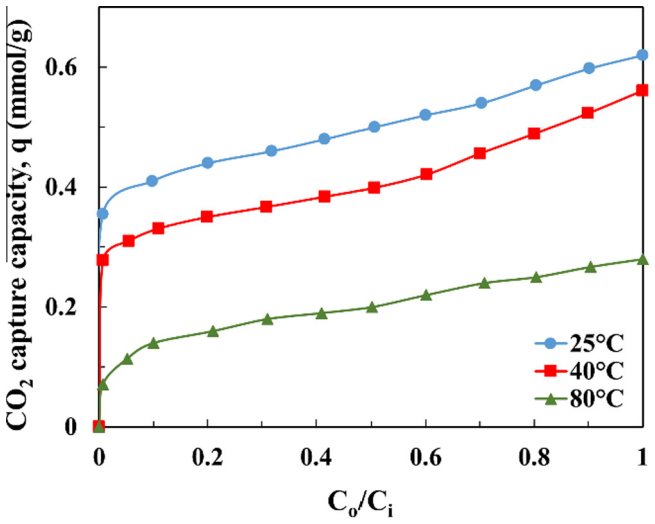

Fig. 11. The effect of temperature on CO_2 adsorption capacity of s.b.9. The inlet gas flow rate was 130 mL/min for all three measurements.

reported by Chen et al. [64] (0.63 mmol/g at 0.15 bar and 25 °C), but lower than that of sulfonate-grafted porous polymer networks (PPNs) reported by Lu et al. [65] (1.12 mmol/g at 0.15 bar and 25 °C).

4. Conclusions

Novel molecularly imprinted poly(AAm-co-EGDMA) spherical particles were synthesized by suspension polymerization in an oil-in-water emulsion and used for CO_2 adsorption from a CO_2/N_2 gas mixture. The ability of the particles to adsorb CO_2 was closely related to their hierarchical porous structure characterized by the mesopores formed by phase separation and the nanocavities smaller than 1 nm with CO_2 recognition properties formed by molecular imprinting. The nitrogen adsorption-desorption isotherms for most of the samples were of type IV, featuring uniform pore size distribution and a BET surface area up to 457 m^2/g, which facilitated the diffusion of CO_2 through the polymer matrix and improved accessibility of the cavities to CO_2 molecules. The poor correlation between CO_2 capture capacity and total volume of the mesopores reflected the fact that the CO_2 adsorption capacity depended primarily on the quality and number of nanocavities, which were too small (d < 1 nm) to be detected by the BET analysis but their presence was revealed by employing the HK method.

Higher contents of functional monomer (AAm) and low-polar solvent (TL) in the organic phase prior to polymerization led to higher CO_2 capture capacity of the particles due to stronger hydrogen bonding interactions between the template and the monomer during complex formation and larger number of CO_2-philic NH_2 moieties in the polymer network. The fraction of nitrogen on the surface of the particles increased by increasing the dispersed phase content in the reactor and the concentration of acrylamide, but excessive acrylamide concentration and/or dispersed phase content led to gelation of the continuous phase and failure of the polymerization process.

The particle size was controlled by changing the agitation rate in the reactor and the surfactant concentration in the aqueous phase. The particles exhibited good thermal stability with a 5% weight loss at 240–255 °C and the maximum equilibrium CO_2 adsorption capacity of 0.56 and 0.62 mmol/g at 40 °C and 25 °C, respectively, and 0.15 bar CO_2 partial pressure. The particle size and density were within the range suitable for applications in fixed bed and fluidized bed adsorption systems. In addition, suspension

polymerization approach significantly facilitates the production scale-up, compared to bulk polymerization.

Acknowledgements

The authors gratefully acknowledge the financial support for this work by coERCe granted by Innovate UK, project Grant: 102213, and Cambridge Engineering and Analysis Design (CEAD) Ltd. The authors would like to thank Sean Creedon, Tony Eyre, Monika Pietrzak, Rob Bentham, Tim Coles, and Kim Robertshaw for their help and support during the entire experimental work.

Appendix A. Supplementary data

Supplementary data associated with this article can be found, in the online version, at http://dx.doi.org/10.1016/j.cej.2016.07.054.

References

[1] N. MacDowell, N. Florin, A. Buchard, J. Hallett, A. Galindo, G. Jackson, et al., An overview of CO_2 capture technologies, Energy Environ. Sci. 3 (2010) 1645–1669.
[2] J. Wang, L. Huang, R. Yang, Z. Zhang, J. Wu, Y. Gao, et al., Recent advances in solid sorbents for CO_2 capture and new development trends, Energy Environ. Sci. 7 (2014) 3478–3518.
[3] IEA, Technology Roadmap: Carbon Capture and Storage, International Energy Agency (IEA), Paris, 2013.
[4] D.Y.C. Leung, G. Caramanna, M.M. Maroto-Valer, An overview of current status of carbon dioxide capture and storage technologies, Renew. Sustain. Energy Rev. 39 (2014) 426–443.
[5] E.S. Rubin, H. Mantripragada, A. Marks, P. Versteeg, J. Kitchin, The outlook for improved carbon capture technology, Prog. Energy Combust. Sci. 38 (2012) 630–671.
[6] A.A. Olajire, CO_2 capture and separation technologies for end-of-pipe applications – a review, Energy 35 (2010) 2610–2628.
[7] S.D. Kenarsari, D. Yang, G. Jiang, S. Zhang, J. Wang, A.G. Russell, et al., Review of recent advances in carbon dioxide separation and capture, RSC Adv. 3 (2013) 22739–22773.
[8] R. Sabouni, H. Kazemian, S. Rohani, Carbon dioxide capturing technologies: a review focusing on metal organic framework materials (MOFs), Environ. Sci. Pollut. Res. 21 (2014) 5427–5449.
[9] J.D. Figueroa, T. Fout, S. Plasynski, H. McIlvried, R.D. Srivastava, Advances in CO_2 capture technology – the U.S. Department of Energy's carbon sequestration program, Int. J. Greenhouse Gas Control 2 (2008) 9–20.
[10] G.T. Rochelle, Amine scrubbing for CO_2 capture, Science 325 (2009) 1652–1654.
[11] C.H. Yu, A review of CO_2 capture by absorption and adsorption, Aerosol Air Qual. Res. 12 (2012) 745–769.
[12] E.F. da Silva, A.M. Booth, Emissions from postcombustion CO_2 capture plants, Environ. Sci. Technol. 47 (2013) 659–660.
[13] A. Schäffer, K. Brechtel, G. Scheffknecht, Comparative study on differently concentrated aqueous solutions of MEA and TETA for CO_2 capture from flue gases, Fuel 101 (2012) 148–153.
[14] M. Karl, R.F. Wright, T.F. Berglen, B. Denby, Worst case scenario study to assess the environmental impact of amine emissions from a CO_2 capture plant, Int. J. Greenhouse Gas Control 5 (2011) 439–447.
[15] G. Qi, Y. Wang, L. Estevez, X. Duan, N. Anako, A.H.A. Park, et al., High efficiency nanocomposite sorbents for CO_2 capture based on amine-functionalized mesoporous capsules, Energy Environ. Sci. 4 (2011) 444–452.
[16] D.M. D'Alessandro, B. Smit, J.R. Long, Carbon dioxide capture: prospects for new materials, Angew. Chem. Int. Ed. 49 (2010) 6058–6082.
[17] Y.-J. Lin, G.T. Rochelle, Approaching a reversible stripping process for CO_2 capture, Chem. Eng. J. 283 (2016) 1033–1043.
[18] T.M. McDonald, W.R. Lee, J.A. Mason, B.M. Wiers, C.S. Hong, J.R. Long, Capture of carbon dioxide from air and flue gas in the alkylamine-appended metal-organic framework mmen-Mg 2(dobpdc), J. Am. Chem. Soc. 134 (2012) 7056–7065.
[19] S. Choi, J.H. Drese, C.W. Jones, Adsorbent materials for carbon dioxide capture from large anthropogenic point sources, ChemSusChem 2 (2009) 796–854.
[20] M.E. Boot-Handford, J.C. Abanades, E.J. Anthony, M.J. Blunt, S. Brandani, N. Mac Dowell, et al., Carbon capture and storage update, Energy Environ. Sci. 7 (2014) 130–189.
[21] J. Yoo, S.H. Cho, T. Yang, Comparison of activated carbon and zeolite 13X for CO_2 recovery from flue gas by pressure swing adsorption, Ind. Eng. Chem. Res. 34 (1995) 591–598.
[22] G. Li, P. Xiao, P. Webley, J. Zhang, R. Singh, M. Marshall, Capture of CO_2 from high humidity flue gas by vacuum swing adsorption with zeolite 13X, Adsorption 14 (2008) 415–422.
[23] P.J.E. Harlick, A. Sayari, Applications of pore-expanded mesoporous silicas. 3. Triamine silane grafting for enhanced CO_2 adsorption, Ind. Eng. Chem. Res. 45 (2006) 3248–3255.
[24] L. Wang, M. Yao, X. Hu, G. Hu, J. Lu, M. Luo, et al., Amine-modified ordered mesoporous silica: the effect of pore size on CO_2 capture performance, Appl. Surf. Sci. 324 (2015) 286–292.
[25] V. Zelenák, M. Badanicová, D. Halamová, J. Cejka, A. Zukal, N. Murafa, et al., Amine-modified ordered mesoporous silica: effect of pore size on carbon dioxide capture, Chem. Eng. J. 144 (2008) 336–342.
[26] Z. Chen, S. Deng, H. Wei, B. Wang, J. Huang, G. Yu, Polyethylenimine-impregnated resin for high CO_2 adsorption: an efficient adsorbent for CO_2 capture from simulated flue gas and ambient air, ACS Appl. Mater. Interfaces 5 (2013) 6937–6945.
[27] J. Duan, M. Higuchi, R. Krishna, T. Kiyonaga, Y. Tsutsumi, Y. Sato, et al., High $CO_2/N_2/O_2/CO$ separation in a chemically robust porous coordination polymer with low binding energy, Chem. Sci. 5 (2014) 660–666.
[28] M.B. Yue, L.B. Sun, Y. Cao, Y. Wang, Z.J. Wang, J.H. Zhu, Efficient CO_2 capturer derived from As-synthesized MCM-41 modified with amine, Chem. Eur. J. 14 (2008) 3442–3451.
[29] S. Choi, J.H. Drese, P.M. Eisenberger, C.W. Jones, Application of amine-tethered solid sorbents for direct CO_2 capture from the ambient air, Environ. Sci. Technol. 45 (2011) 2420–2427.
[30] R. Serna-Guerrero, E. Da'na, A. Sayari, New insights into the interactions of CO_2 with amine-functionalized silica, Ind. Eng. Chem. Res. 47 (2008) 9406–9412.
[31] F.Q. Liu, L. Wang, Z.G. Huang, C.Q. Li, W. Li, R.X. Li, et al., Amine-tethered adsorbents based on three-dimensional macroporous silica for CO_2 capture from simulated flue gas and air, ACS Appl. Mater. Interfaces 6 (2014) 4371–4381.
[32] N. Hiyoshi, K. Yogo, T. Yashima, Adsorption of carbon dioxide on amine modified SBA-15 in the presence of water vapor, Chem. Lett. 33 (2004) 510–511.
[33] R. Serna-Guerrero, Y. Belmabkhout, A. Sayari, Further investigations of CO_2 capture using triamine-grafted pore-expanded mesoporous silica, Chem. Eng. J. 158 (2010) 513–519.
[34] M. Eddaoudi, J. Kim, N. Rosi, D. Vodak, J. Wachter, M. O'Keeffe, et al., Systematic design of pore size and functionality in isoreticular MOFs and their application in methane storage, Science 295 (2002) 469–472.
[35] M.A. Habib, H.M. Badr, S.F. Ahmed, R. Ben-Mansour, K. Mezghani, S. Imashuku, et al., A review of recent developments in carbon capture utilizing oxy-fuel combustion in conventional and ion transport membrane systems, Int. J. Energy Res. 35 (2011) 741–764.
[36] W. Lu, J.P. Sculley, D. Yuan, R. Krishna, Z. Wei, H.C. Zhou, Polyamine-tethered porous polymer networks for carbon dioxide capture from flue gas, Angew. Chem. Int. Ed. 51 (2012) 7480–7484.
[37] K. Sumida, D.L. Rogow, J.A. Mason, T.M. McDonald, E.D. Bloch, Z.R. Herm, et al., Carbon dioxide capture in metal-organic frameworks, Chem. Rev. 112 (2012) 724–781.
[38] J. Donald Carruthers, M.A. Petruska, E.A. Sturm, S.M. Wilson, Molecular sieve carbons for CO_2 capture, Microporous Mesoporous Mater. 154 (2012) 62–67.
[39] J. Liu, N. Sun, C. Sun, H. Liu, C. Snape, K. Li, et al., Spherical potassium intercalated activated carbon beads for pulverised fuel CO_2 post-combustion capture, Carbon 94 (2015) 243–255.
[40] S. Deng, H. Wei, T. Chen, B. Wang, J. Huang, G. Yu, Superior CO_2 adsorption on pine nut shell-derived activated carbons and the effective micropores at different temperatures, Chem. Eng. J. 253 (2014) 46–54.
[41] J. Cai, J. Qi, C. Yang, X. Zhao, Poly(vinylidene chloride)-based carbon with ultrahigh microporosity and outstanding performance for CH_4 and H_2 storage and CO_2 capture, ACS Appl. Mater. Interfaces 6 (2014) 3703–3711.
[42] X. Fan, L. Zhang, G. Zhang, Z. Shu, J. Shi, Chitosan derived nitrogen-doped microporous carbons for high performance CO_2 capture, Carbon 61 (2013) 423–430.
[43] G. Sethia, A. Sayari, Nitrogen-doped carbons: remarkably stable materials for CO_2 capture, Energy Fuels 28 (2014) 2727–2731.
[44] T. Ben, C. Pei, D. Zhang, J. Xu, F. Deng, X. Jing, et al., Gas storage in porous aromatic frameworks (PAFs), Energy Environ. Sci. 4 (2011) 3991–3999.
[45] C.F. Martín, E. Stöckel, R. Clowes, D.J. Adams, A.I. Cooper, J.J. Pis, et al., Hypercrosslinked organic polymer networks as potential adsorbents for pre-combustion CO_2 capture, J. Mater. Chem. 21 (2011) 5475–5483.
[46] Z. Xiang, X. Zhou, C. Zhou, S. Zhong, X. He, C. Qin, et al., Covalent-organic polymers for carbon dioxide capture, J. Mater. Chem. 22 (2012) 22663–22669.
[47] Y. Zhao, Y. Shen, L. Bai, R. Hao, L. Dong, Synthesis and CO_2 adsorption properties of molecularly imprinted adsorbents, Environ. Sci. Technol. 46 (2012) 1789–1795.
[48] Y. Zhao, Y. Shen, G. Ma, R. Hao, Adsorption separation of carbon dioxide from flue gas by a molecularly imprinted adsorbent, Environ. Sci. Technol. 48 (2014) 1601–1608.
[49] L. Chen, S. Xu, J. Li, Recent advances in molecular imprinting technology: current status, challenges and highlighted applications, Chem. Soc. Rev. 40 (2011) 2922–2942.
[50] B. Brooks, Suspension polymerization processes, Chem. Eng. Technol. 33 (2010) 1737–1744.
[51] B. Dirion, Z. Cobb, E. Schillinger, L.I. Andersson, B. Sellergren, Water-compatible molecularly imprinted polymers obtained via high-throughput synthesis and experimental design, J. Am. Chem. Soc. 125 (2003) 15101–15109.
[52] Q.Q. Gai, F. Qu, Z.J. Liu, R.J. Dai, Y.K. Zhang, Superparamagnetic lysozyme surface-imprinted polymer prepared by atom transfer radical polymerization

and its application for protein separation, J. Chromatogr. A 1217 (2010) 5035–5042.
[53] E.G. Derouane, Catalysts for Fine Chemical Synthesis: Microporous and Mesoporous Solid Catalysts, first ed., John Wiley & Sons Ltd., West Sussex, 2006.
[54] D. Geldart, Types of gas fluidization, Powder Technol. 7 (1973) 285–292.
[55] R.G. Holdich, Fundamentals of Particle Technology, first ed., Midland Information Technology and Publishing, Loughborough, 2002.
[56] Z. Wang, M. Kwauk, H. Li, Fluidization of fine particles, Chem. Eng. Sci. 53 (1998) 377–395.
[57] B. Sreenivasulu, I. Sreedhar, P. Suresh, K.V. Raghavan, Development trends in porous adsorbents for carbon capture, Environ. Sci. Technol. 49 (2015) 12641–12661.
[58] G. Odian, Principles of Polymerization, fourth ed., John Wiley & Sons Inc., New York, 2004.
[59] H. Yan, K.H. Row, Characteristic and synthetic approach of molecularly imprinted polymer, Int. J. Mol. Sci. 7 (2006) 155–178.
[60] M.H. Mohamed, L.D. Wilson, Porous copolymer resins: tuning pore structure and surface area with non reactive porogens, Nanomaterials 2 (2012) 163–186.
[61] R. Dawson, D.J. Adams, A.I. Cooper, Chemical tuning of CO_2 sorption in robust nanoporous organic polymers, Chem. Sci. 2 (2011) 1173–1177.
[62] M. Kaliva, G.S. Armatas, M. Vamvakaki, Microporous polystyrene particles for selective carbon dioxide capture, Langmuir 28 (2012) 2690–2695.
[63] H.A. Patel, S.H. Je, J. Park, D.P. Chen, Y. Jung, C.T. Yavuz, et al., Unprecedented high-temperature CO_2 selectivity in N_2-phobic nanoporous covalent organic polymers, Nat. Commun. 4 (2013) 1357–1364.
[64] D. Chen, S. Gu, Y. Fu, Y. Zhu, C. Liu, G. Li, et al., Tunable porosity of nanoporous organic polymers with hierarchical pores for enhanced CO_2 capture, Polym. Chem. (2016) 3416–3422.
[65] W. Lu, D. Yuan, J. Sculley, D. Zhao, R. Krishna, H.-C. Zhou, Sulfonate-grafted porous polymer networks for preferential CO_2 adsorption at low pressure, J. Am. Chem. Soc. 133 (2011) 18126–18129.